Efficient Deconvolution and Super-Resolution Methods in Microwave Imagery

Igor Yanovsky, Bjorn H. Lambrigtsen, Alan B. Tanner and Luminita A. Vese

***Abstract*—In this paper, we develop efficient deconvolution and super-resolution methodologies and apply these techniques to reduce image blurring and distortion inherent in an aperture synthesis system. Such a system produces ringing at sharp edges and other transitions in the observed field. The conventional approach to suppressing sidelobes is to apply linear apodization, which has the undesirable side effect of degrading spatial resolution. We have developed an efficient total variation minimization technique based on Split Bregman deconvolution that reduces image ringing while sharpening the image and preserving information content. The model was generalized to include upsampling of deconvolved images to a higher resolution grid. Furthermore, a proposed multiframe super-resolution method is presented that is robust to image noise and noise in the point spread function and leads to additional improvements in spatial resolution. Our super-resolution methodologies are based on current research in sparse optimization and compressed sensing, which lead to unprecedented efficiencies for solving image reconstruction problems.**

***Index Terms*—Aperture synthesis system, inverse problems, microwave imaging, remote sensing, sparse optimization, spatial resolution, super-resolution.**

I. Introduction

HURRICANES and other physically deforming weather phenomena will soon be continuously imaged using geostationary microwave sensors, which are designed to penetrate through thick clouds to see the structure of a storm. Such images may represent distribution of temperature, water vapor, and cloud liquid water and are valuable for evaluating the storm's internal processes and its strength. The Geostationary Synthetic Thinned Aperture Radiometer (GeoSTAR) is a microwave spectrometer aperture synthesis system that has been under development at JPL since 1998 [1] and will be used to capture hurricane imagery. The instrument concept consists of an array of individual microwave receivers arranged in a Y-pattern in a plane facing the Earth. Each receiver has a small feedhorn antenna, which views the entire Earth disc, and the received signal is processed on-board to determine the cross-correlation between pairs of receivers. The cross-correlations, called visibilities, are equivalent to coefficients of a complex 2-dimensional Fourier series that represents the radiometric image of the Earth disc. The visibilities are measured between all receiver pairs simultaneously and accumulated on-board for a period of a few seconds before being downlinked to the ground for further processing. There, the visibility images are converted to radiometric images, essentially through an inverse Fourier transform (Fig. 1). GeoSTAR will acquire earth imagery continuously, but will require a full 15 minutes to achieve its full radiometric sensitivity (NEDT) of 0.3 Kelvin. Imagery will also be available with higher time resolution of 1 minute, but with a degraded NEDT of 1.2 Kelvin.

A characteristic of an aperture synthesis system is that the point spread function (PSF) is a 2-dimensional sinc-like function, showing positive and negative excursions (Fig. 2), that produces ringing at sharp edges and other transitions in the observed field. The conventional approach to suppressing sidelobes is to apply linear apodization, which has the undesirable side effect of degrading spatial resolution [2].

In order to reduce image ringing while sharpening the image and preserving information content, we take a different approach by formally solving the deconvolution inverse problem. Since the convolution problem in the presence of noise is highly ill-posed, regularization is applied to achieve stability while preserving a priori properties of the solution. We formulate the restoration problem within the variational framework, using the total variation regularization [3]. Total variation (TV) of an image measures the sum of the absolute values of its gradient and increases in the presence of the ringing artifact caused by sidelobes. By minimizing the TV of an image using the numerical techniques detailed below, our process reduces not only the ringing within the image, but is shown to significantly reduce the brightness temperature errors in the overall image. To render these processes efficiently, our methodologies are based on current research in sparse optimization and compressed sensing. We perform the total variation based deconvolution within the Split Bregman optimization framework to achieve a factor of five hundred computational time improvement over already robust total-variation gradient descent based techniques. Additionally, proposed upsampling, as well as a multiframe super-resolution method that is robust to image noise and noise in the point spread function, lead to additional improvements in spatial resolution.

This work was supported by the National Aeronautics and Space Administration (NASA), Weather Research program. The work of I. Yanovsky and L. A. Vese was also supported by the National Science Foundation under Grant DMS 1217239.

I. Yanovsky is with the Jet Propulsion Laboratory, California Institute of Technology, Pasadena, CA 91109 USA, and also with the Joint Institute for Regional Earth System Science and Engineering, University of California, Los Angeles, CA 90095 USA (e-mail: igor.yanovsky@jpl.nasa.gov).

A. Tanner and B. Lambrigtsen are with the Jet Propulsion Laboratory, California Institute of Technology, CA 91109 USA.

L. Vese is with the Department of Mathematics, University of California, Los Angeles, CA 90095 USA.

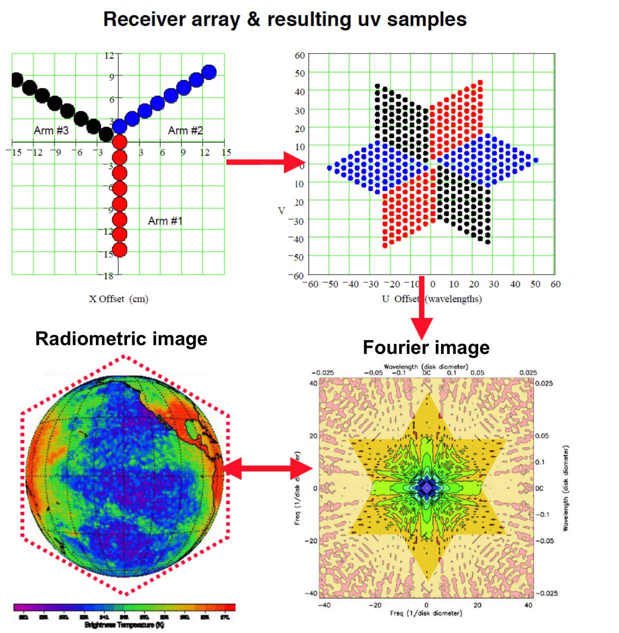

Fig. 1. Sparse array (upper left) and u-v sampling pattern (upper right), as implemented in the GeoSTAR prototype. Typical visibility magnitudes in the uv-plane (lower-right) correspond to the radiometric image (lower-left). Red, blue, and black colors of the u-v samples correspond to pairings of elements from arms 1-2, 2-3, and 3-1, respectively.

II. Notation

We first introduce notations that will be used throughout this paper. For an image $u \in \mathbb{R}^{n\times n}$, the value of u at a pixel (i,j), with $0 \le i,j \le n$, is denoted as u_{ij}. The norms are defined as:

$$||u||_1 = \sum_{(i,j)\in\Omega} |u_{ij}|, \qquad ||u||_2 = \sqrt{\sum_{(i,j)\in\Omega} |u_{ij}|^2}.$$

The gradient of u is denoted as ∇u and its value at pixel (i,j) as ∇u_{ij}, with $\nabla u_{ij} \in \mathbb{R}^2$. For a vector-valued quantity $\mathbf{d}_{ij} = ((d_1)_{ij}, (d_2)_{ij}) \in \mathbb{R}^2$, for example $\mathbf{d} = \nabla u$, the norms are defined as

$$||\mathbf{d}||_1 = \sum_{(i,j)\in\Omega} ||\mathbf{d}_{ij}||_2, \qquad ||\mathbf{d}||_2 = \sqrt{\sum_{(i,j)\in\Omega} ||\mathbf{d}_{ij}||_2^2},$$

where $||\mathbf{d}_{ij}||_2 = \sqrt{(d_1)_{ij}^2 + (d_2)_{ij}^2}$. Unless specified otherwise, $||\cdot|| = ||\cdot||_2$ in the remainder of this paper.

The following signal-to-noise ratio (SNR) and root mean square error (RMSE) were employed as quantitative measures:

$$\text{SNR} = 10\log_{10}\left(\frac{\sigma_{u_0}^2 \cdot n^2}{||u_0 - u||^2}\right), \tag{1}$$

$$\text{RMSE} = \sqrt{\frac{1}{n^2}\sum_{(i,j)\in\Omega} |u_{0\,ij} - u_{ij}|^2}, \tag{2}$$

where n^2 is the total number of pixels in the image, u_0 represents the original clean image, $\sigma_{u_0}^2$ is the variance of u_0, and u represents the image of interest.

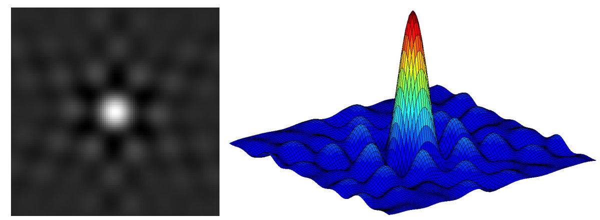

Fig. 2. The GeoSTAR point spread function (PSF). A characteristic of an aperture synthesis system is that the PSF is a 2-dimensional sinc-like function, showing positive and negative excursions, that produces ringing at sharp edges and other transitions in the observed field.

III. Background

The degradation model of an image u_0 we consider is

$$f = Hu_0 + \kappa, \tag{3}$$

where H is an operator characterizing blurring and subsampling, κ is additive noise, and f is an observed image. In case of an aperture synthesis system, H contains a sinc-like convolution operation which introduces sidelobes in the observation. The conventional approach to suppressing sidelobes is to apply linear apodization. However, this approach has the undesirable side effect of degrading spatial resolution [2].

Another approach of suppressing interferometric sidelobes is to construct a variational formulation for image reconstruction and solve an inverse problem. Since problem (3) is highly ill-posed, regularization should be applied within a variational framework in order to achieve stability while preserving a priori properties of the solution.

Variational methods play a very important role in image analysis since they allow for accurate and dense estimation of the solution to an ill-posed problem. Variational techniques are based on the minimization of a functional that consists of a similarity term $F(Hu - f)$ that preserves certain features in the data, and a regularization term $R(u)$ that regularizes the non-unique solution by an additional smoothness assumption. The general minimization problem for reconstructing u, which is an approximation of u_0, can be written as:

$$\min_u \{R(u) + F(Hu - f)\}. \tag{4}$$

Several regularization terms have been presented in the literature, including [4]–[7]. Also, new image restoration models, based on non-local image information, have been developed [8]–[12], which have proved successful in medical imaging and computational photography applications. In particular, [13] introduced the nonlocal means filter for image denoising, and in [8], [9], [14], the authors formulated a variational framework by proposing nonlocal regularizing functionals. In [15], [16], the authors proposed an approach that uses the Mumford-Shah model [17] and nonlocal image information. However, such approaches are very computationally expensive.

We formulate the restoration problem within the variational framework, using the total variation regularization. The L_1-regularized type norm $||u||_{TV}$ measures the total variation (TV) of a signal, and is defined as

$$||u||_{TV} = \int |\nabla u|.$$

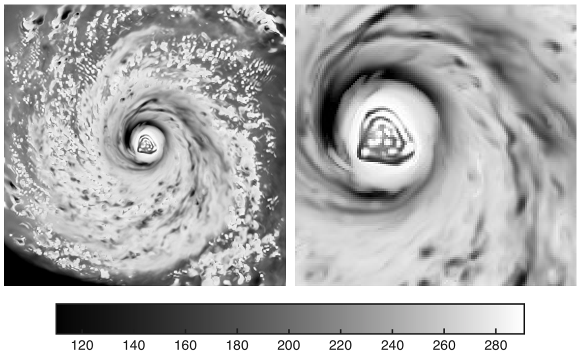

Fig. 3. Original 150GHz microwave 400x400 pixel image of the simulated hurricane Rita and its zoomed in region are shown. The units on color bar are in Kelvin. The spatial resolution of the model used to produce the simulation is 1.9 km.

The discrete total variation is given as

$$||u||_{TV} = ||\nabla u||_1 = \sum_{(i,j)\in\Omega} ||\nabla u_{ij}||. \tag{5}$$

The TV norm was originally proposed for image denoising and deblurring [3], [18] and had since been used to solve a variety of image reconstruction problems. The effectiveness of the TV norm stems from its ability to preserve edges in an image.

In [19], [20], the authors proposed fast operator-splitting and alternating minimization methods for solving TV-L^2 deconvolution problems. Also, the Split Bregman algorithm for denoising images was proposed in [21]. In their paper, the authors show that the Bregman iteration can be used to solve rapidly and accurately a wide variety of constrained optimization problems. These formulations are related to problems that arise frequently in compressed sensing, where function u is reconstructed from a small subset of its Fourier coefficients [22]–[24]. Inspired by these methodologies, we minimize the deconvolution and super resolution problems within the Split Bregman minimization framework.

IV. Fast Split Bregman Deconvolution

A deconvolution process reverses the effects of a blurring sensor point spread function (PSF) on observed data in the presence of noise. It is also an important step in multiframe super-resolution.

Let $u_0 \in \mathbb{R}^{n\times n}$ be an original unknown image, K be a convolution operator that represents the point spread function, and $\kappa \in \mathbb{R}^{n\times n}$ be additive noise. A blurred, distorted, and noisy observation f satisfies the model

$$f = K * u_0 + \kappa. \tag{6}$$

The convolution model (6) is a specific case of (3). The restoration problem is formulated within the variational framework, with the total variation (5) as a regularization. Given a single observation f, we solve the inverse problem. The minimization problem for TV-L_2 deconvolution can be written as

$$\min_u \; ||u||_{TV} + \frac{\mu}{2}||K * u - f||_2^2, \tag{7}$$

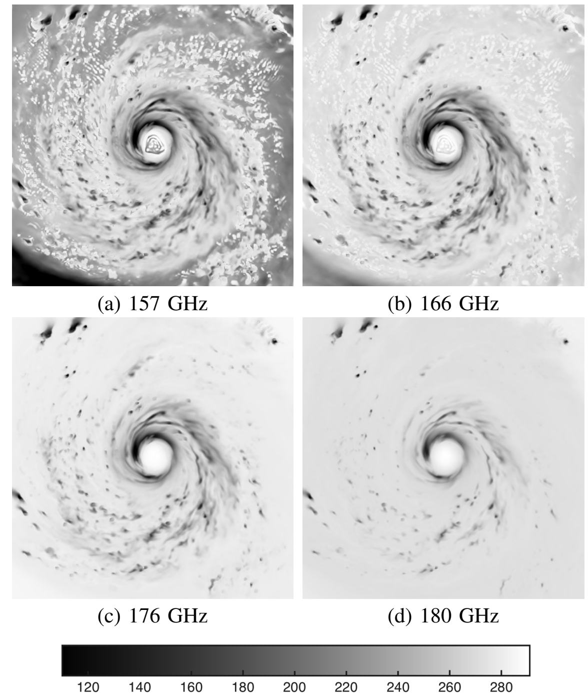

Fig. 4. Original four microwave channels (157, 166, 176, and 180 GHz) of the simulated hurricane Rita image. These four channels correspond to the AMSU-B water vapor sounding channels, which are placed progressively closer to the 183 GHz water vapor resonance frequency to provide a range of penetration depths. These channels are later combined with temperature profiles to resolve the vertical distribution of water vapor in the atmosphere. The 150GHz channel is shown in Figure 3. The units on color bar are in Kelvin.

where u is a reconstruction and $\mu > 0$ is a weight on the L_2 norm of the residual of (6). The value of μ can be calculated automatically via Bregman iteration [25], [26].

In order to minimize (7), an additional variable $\mathbf{d}$ is introduced to transfer ∇u out of non-differentiable terms at each pixel, and $||\mathbf{d} - \nabla u||^2$ is penalized. Hence, the Split Bregman formulation of the problem (7) is

$$\min_{u,\mathbf{d}} \quad ||\mathbf{d}||_1 + \frac{\lambda}{2}||\mathbf{d} - \nabla u - \mathbf{b}||^2 + \frac{\mu}{2}||K * u - f||^2. \tag{8}$$

Here, λ is a nonnegative parameter, and variable $\mathbf{b}$ is chosen through Bregman iteration [25], [26]:

$$\mathbf{b} \quad \leftarrow \quad \mathbf{b} + (\nabla u - \mathbf{d}).$$

For a fixed u, the minimization problem for $\mathbf{d}$ is

$$\mathbf{d}^* = \arg\min_{\mathbf{d}} \; \left\{ ||\mathbf{d}||_1 + \frac{\lambda}{2}||\mathbf{d} - \nabla u - \mathbf{b}||^2 \right\},$$

which can be explicitly solved for $\mathbf{d}$, at each pixel, by using a generalized shrinkage formula [27], [28]:

$$\mathbf{d} \;=\; \max\left\{||\nabla u + \mathbf{b}|| - \frac{1}{\lambda}, 0\right\}\frac{\nabla u + \mathbf{b}}{||\nabla u + \mathbf{b}||}.$$

For a fixed $\mathbf{d}$, the minimization problem (8) is quadratic in u:

$$u^* \;=\; \arg\min_u \; \left\{ ||\mathbf{d} - \nabla u - \mathbf{b}||^2 + \frac{\mu}{\lambda}||K * u - f||^2 \right\},$$

and has the optimality condition:

$$\mu\tilde{K} * K * u - \lambda\triangle u = \mu\tilde{K} * f - \lambda\nabla\cdot(\mathbf{d} - \mathbf{b}), \tag{9}$$

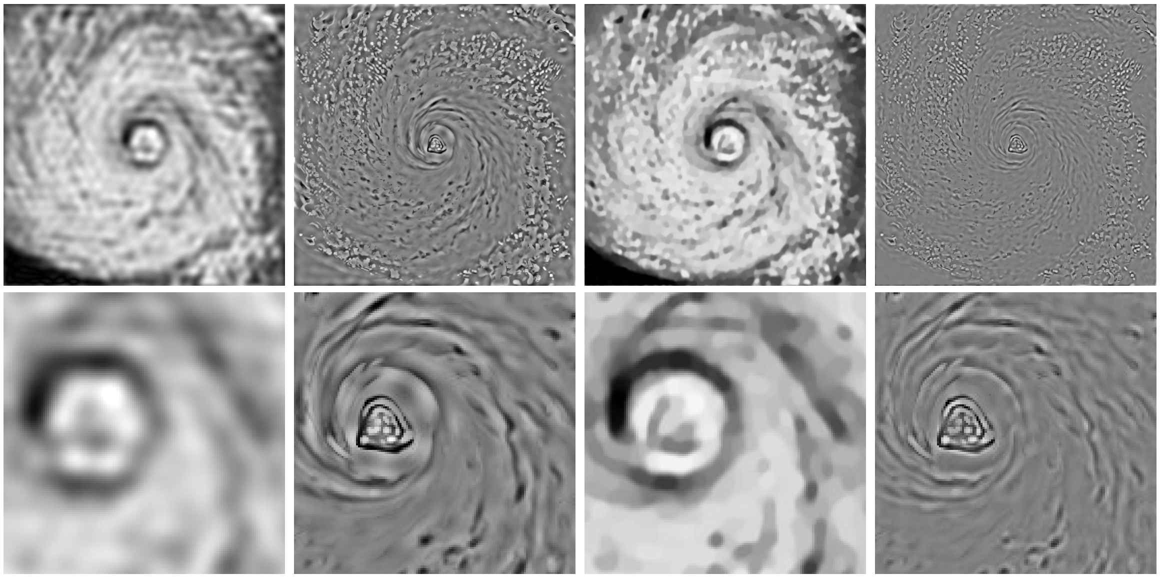

(a) Blurry and noisy 150GHz image (b) Original Error. SNR = 5.98, RMSE = 20.46K (c) Reconstruction (d) Final Error. SNR = 8.77, RMSE = 14.85K

Fig. 5. Split Bregman deconvolution of a simulated 150 GHz hurricane image. (a) Original image from Figure 3 is convolved with the GeoSTAR kernel from Figure 2. (b) Error between clean image and blurry image. (c) Deconvolution result. (d) Error between clean image and deconvolution result.

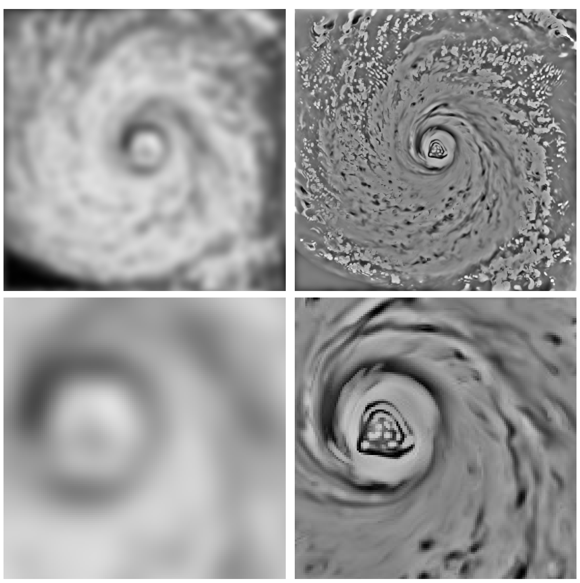

(a) Apodization result (b) Error. SNR = 4.78, RMSE = 23.50K

Fig. 6. (a) Result obtained after applying the conventional linear apodization method on image of Figure 5(a). (b) Corresponding error is shown. Linear apodization method raises the errors relative to Figure 5(b).

where $\tilde{K}(x) = K(-x)$. Similar to [19], we solve (9) using the fast Fourier transform:

$$u = \mathcal{F}^{-1}\left(\frac{\mathcal{F}\left(\mu\tilde{K} * f - \lambda\nabla\cdot(\mathbf{d}-\mathbf{b})\right)}{\mathcal{F}\left(\mu\tilde{K} * K - \lambda\triangle\right)}\right).$$

We tested the method on simulated microwave 150, 157, 166, 176, and 180 GHz channel images of the 2005 Atlantic hurricane Rita, shown in Figures 3 and 4. For comparison, GeoSTAR operates at some of the same frequencies of the Advanced Microwave Sounding Unit - B (AMSU-B) temperature and humidity sounders near 55 GHz and 180 GHz, respectively. The images are 400 by 400 pixels and were derived from cloud resolving numerical weather prediction model (WRF) [29] simulations. The resolution of a pixel is 1.9 km. We used the 101 by 101 GeoSTAR point spread function K, which has a full width at half maximum of 27.6 km and is shown in Figure 2, to blur the images.

Figure 5(a) shows the 150 GHz image of Figure 3 degraded with the GeoSTAR blur. The result in Figure 5(c) is obtained using the efficient Split Bregman deconvolution model. Figures 5(b,d) show the original error and error after reconstruction as well as give signal-to-noise ratio (SNR) and root mean square (RMS) error values (see (1) and (2)). These error measures are relative to the original image in Figure 3. In Figures 5(a,b) we see how the GeoSTAR PSF renders an image which tends to "ring" spatially to produce an unnatural appearance. In Figure 5(c), the proposed technique has produced an image which not only appears to match the true image, but in Figure 5(d) truly reduces image errors compared to Figure 5(b). Such error reductions are not realized by apodization (see Figure 6), which in fact raises the errors relative to Figure 5(b) [2].

Figure 7 shows reconstruction results for other (157, 166, 176, and 180 GHz) channels. Table I shows SNR ratios and Table II shows RMS errors for each of the five channels before and after reconstruction. These error measures are relative to the original images in Figures 3 and 4.

We also assessed computational efficiency of the fast fourier transform-based Split Bregman deconvolution method. Alternatively, a standard way of minimizing energy functional (7) is to use the gradient descent method. We found that solving the deconvolution problem using the fast Split Bregman method is over five hundred times faster than using the gradient descent

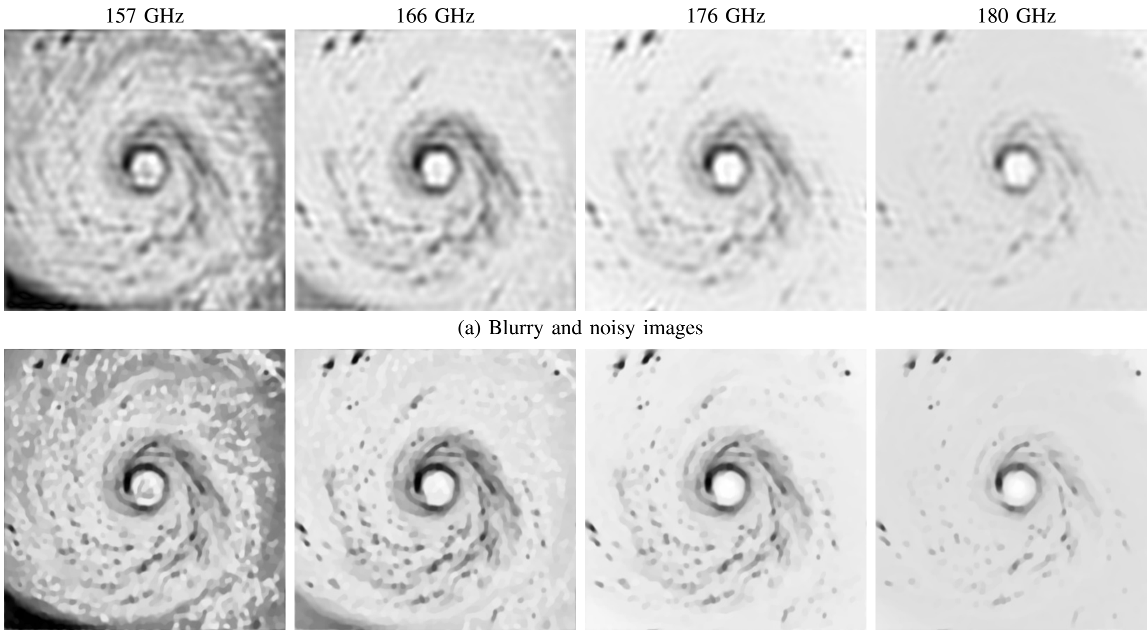

(a) Blurry and noisy images

(b) Reconstruction

Fig. 7. Split Bregman deconvolution of simulated hurricane images. The four columns represent different microwave channels, with higher frequencies, representing upper atmosphere, being highly saturated. (a) Original images from Figure 4 are convolved with GeoSTAR kernel from Figure 2. (b) Deconvolution results. Results for the 150GHz channel are shown in Figure 5. SNR and RMSE values for blurry and reconstructed images are listed in Tables I and II, respectively.

TABLE I
SIGNAL-TO-NOISE RATIOS OF BLURRY AND RECONSTRUCTED IMAGES SHOWN IN FIGURES 5 AND 7

Channels	Blurry image	Reconstructed image
150 GHz	5.98	8.77
157 GHz	6.29	9.09
166 GHz	6.84	10.82
176 GHz	7.26	11.91
180 GHz	6.47	11.22

TABLE II
ROOT MEAN SQUARE ERRORS (IN KELVIN) IN BLURRY AND RECONSTRUCTED IMAGES SHOWN IN FIGURES 5 AND 7

Channels	Blurry image	Reconstructed image
150 GHz	20.46	14.85
157 GHz	15.37	11.14
166 GHz	10.49	6.63
176 GHz	8.23	4.82
180 GHz	5.19	3.01

method.

V. SIMULTANEOUS DECONVOLUTION AND UPSAMPLING VIA SPLIT BREGMAN METHOD

In addition to the effects of noise and point spread function, microwave images are inherently of low spatial resolution compared with optical sensors with similar receiving apertures. The pixel size for the Advanced Microwave Sounding Unit (AMSU) microwave sensors ranges from 15 km (AMSU-B) to 50 km (AMSU-A) per pixel at nadir. Thus, for example, a 3000 by 3000 km scene can be represented on a 200x200 grid (for AMSU-B) to as coarse as a 60x60 grid (for AMSU-A). This limits scientific analysis of reconstructed data products. Our objective is to simultaneously (i) increase the effective resolution of the observed image, upsampling the resolution by a factor of at least 2 in each dimension, (ii) reduce the effects of noise, and (iii) preserve the edges and other features in the image. Hence, in the case of AMSU-B measurements, our goal is to recover a deblurred and denoised representation of a scene on a 400x400 grid (7.5 km resolution) from a blurry and noisy representation on a 200x200 grid. A conceptual diagram of the simultaneous deconvolution and upsampling process is shown in Figure 8.

We first describe the forward imaging model, which convolves, adds noise to, and downsamples the physical scene as it is being captured by the sensor. The downsampling process is defined by the downsampling operator. Such an operator is a transformation from a fine (high-resolution) grid to a coarse (low-resolution) grid. We denote the downsampling matrix as $D \in \mathbb{R}^{n\times p}$ with $p = n/k$, where k is the downsampling (or upsampling) factor. The larger the downsampling factor k is, the coarser the resulting grid would be. We assume that a physical scene u_0, when being captured, is convolved with an antenna kernel K, corrupted with noise κ, and then downsampled with an operator D, arriving at the observation $f \in \mathbb{R}^{p\times p}$:

$$f = D^T(K * u_0 + \kappa)D. \tag{10}$$

In order to enhance the effective spatial resolution, we solve the inverse problem. The minimization problem for simulta-

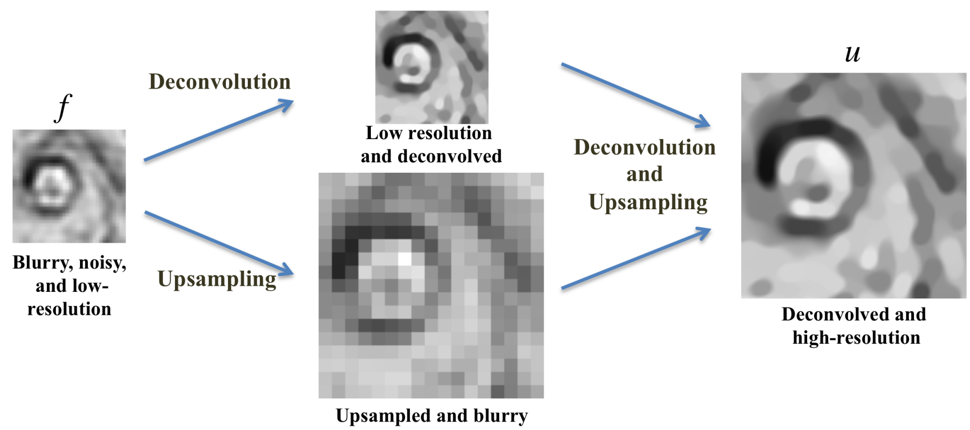

Fig. 8. Conceptual diagram of deconvolution and upsampling process. Deconvolution process, described in Section IV, reverses effects of a blurring sensor point spread function (PSF) on observed data in the presence of noise, reconstructing an image on the same grid as the blurry image. Upsampling process upsamples the blurry image to a finer grid, without performing deconvolution. In simultaneous deconvolution and upsampling, described in Section V, both steps are performed at the same time.

neous deconvolution and upsampling can be written as

$$\min_{u} \ ||\nabla u||_1 + \frac{\mu}{2}||f - D^T(K * u)D||^2, \tag{11}$$

where μ is a nonnegative parameter.

In [15], [16], the authors proposed to solve (10) using the Mumford-Shah model [17] and nonlocal image information. However, such an approach is very computationally expensive. In this paper, we minimize the simultaneous deconvolution and upsampling problem (11), within the Split Bregman minimization framework. We consider the following minimization problem, which is based on a half-quadratic approximation of (11) as

$$\min_{u,\mathbf{d}} \ ||\mathbf{d}||_1 + \frac{\lambda}{2}||\mathbf{d} - \nabla u - \mathbf{b}||^2 + \frac{\mu}{2}||f - D^T(K*u)D||^2. \tag{12}$$

Equations for $\mathbf{b}$ and $\mathbf{d}$ are the same as in Section IV and are therefore omitted. For a fixed $\mathbf{d}$, the minimization problem (12) is quadratic in u:

$$u^* \ = \ \arg\min_{u} \ \frac{\lambda}{2}||\mathbf{d} - \nabla u - \mathbf{b}||^2 + \frac{\mu}{2}||f - D^T(K * u)D||^2.$$

Its optimality condition is given as:

$$\triangle u - \nabla\cdot(\mathbf{d} - \mathbf{b}) + \frac{\mu}{\lambda}\tilde{K} * \Big(D\big(f - D^T(K*u)D\big)D^T\Big) = 0, \tag{13}$$

where $\tilde{K}(x,y) = K(-x,-y)$. Unlike equation (9), equation (13) can not be solved using the fast Fourier Transform due to the presence of operator D. Instead, we parametrize the descent direction by an artificial time t and solve the Euler-Lagrange equation in $u(t)$ using the gradient descent method:

$$\frac{\partial u}{\partial t} = \triangle u - \nabla\cdot(\mathbf{d} - \mathbf{b}) + \frac{\mu}{\lambda}\tilde{K} * \Big(D\big(f - D^T(K*u)D\big)D^T\Big).$$

We tested the Split-Bregman-based simultaneous deconvolution and upsampling method on the 400×400 AMSU-B 150 GHz channel image shown in Figure 3. In order to generate test cases, this image has been blurred with the GeoSTAR point spread function, degraded by Gaussian noise, and downsampled to different resolutions. The downsampling factors were chosen to be $k = 2, 3, 4, 8, 16$, which correspond to downsampling the 400×400 image to 200×200, 134×134, 100×100, 50×50, 25×25 images, respectively (see Figure 9).

TABLE III
SIGNAL-TO-NOISE RATIOS OF DOWNSAMPLED BLURRY AS WELL AS RECONSTRUCTED 150 GHZ IMAGES SHOWN IN FIGURES 9 AND 10

Downsampling factor	Downsampled blurry image	Reconstructed image
k = 1	5.98	8.77
k = 2	5.94	7.74
k = 3	5.87	7.32
k = 4	5.46	7.06
k = 8	4.98	6.33
k = 16	3.93	4.59

After the test cases were generated, the simultaneous deconvolution and upsampling method was used to reconstruct the images back to the original 400×400 grid, as shown in Figure 10. Figure 11 shows errors before and after reconstructions. Table III shows the signal-to-noise ratios and Table IV shows RMS errors of the downsampled and blurry as well as reconstructed images. The first column in each of these tables specifies the factors that were used to downsample images to coarser grids before the reconstruction was performed. The results show that even though the images were significantly corrupted and defined on a coarser grids, the reconstructions look reasonable for k less than or equal to 8. However, for $k = 16$, where each pixel is upsampled to 16^2 pixels, the benefit of the reconstruction, as shown by SNR and RMS error values, is not as significant.

VI. MULTIFRAME SUPER-RESOLUTION

Multiframe super-resolution reconstruction produces a high-resolution image from a sequence of blurry and noisy low-resolution images. We assume we are given Q noisy and blurry observations f_k, where $k = 1, \ldots, Q$. If the point spread function K contains noise s_k, the convolution model describing the relation between the unknown image u_0 and

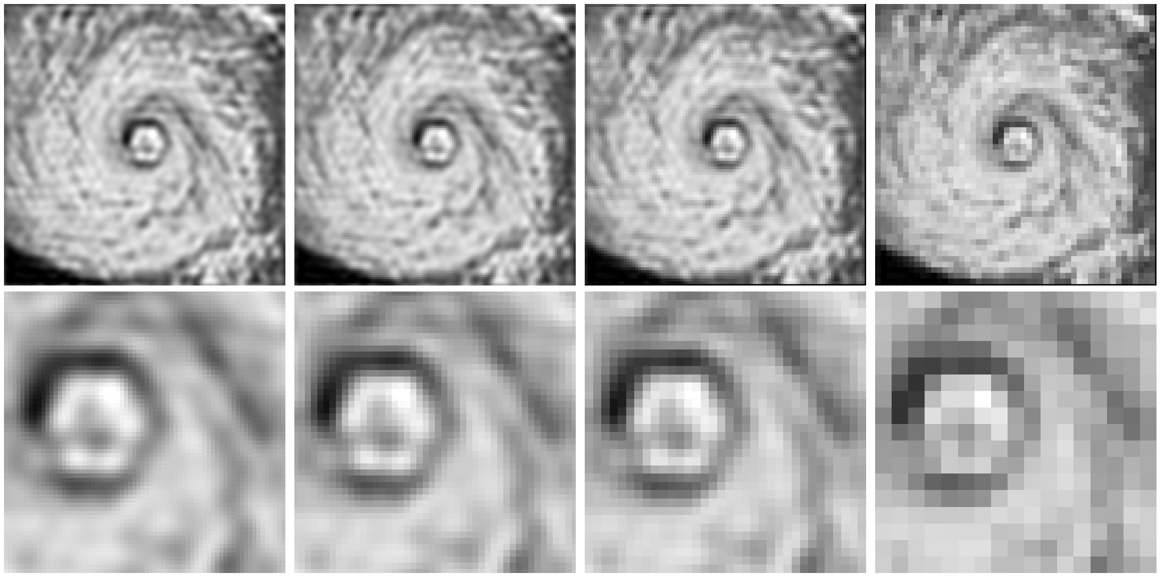

(a) 200x200 image ($k = 2$) (b) 134x134 image ($k = 3$) (c) 100x100 image ($k = 4$) (d) 50x50 image ($k = 8$)

Fig. 9. Image (150 GHz channel) from Figure 3 has been blurred with GeoSTAR kernel from Figure 2, degraded by Gaussian noise, and downsampled to different resolutions. Full size images are shown on the first row, and zoomed in region of each image is shown in the second row.

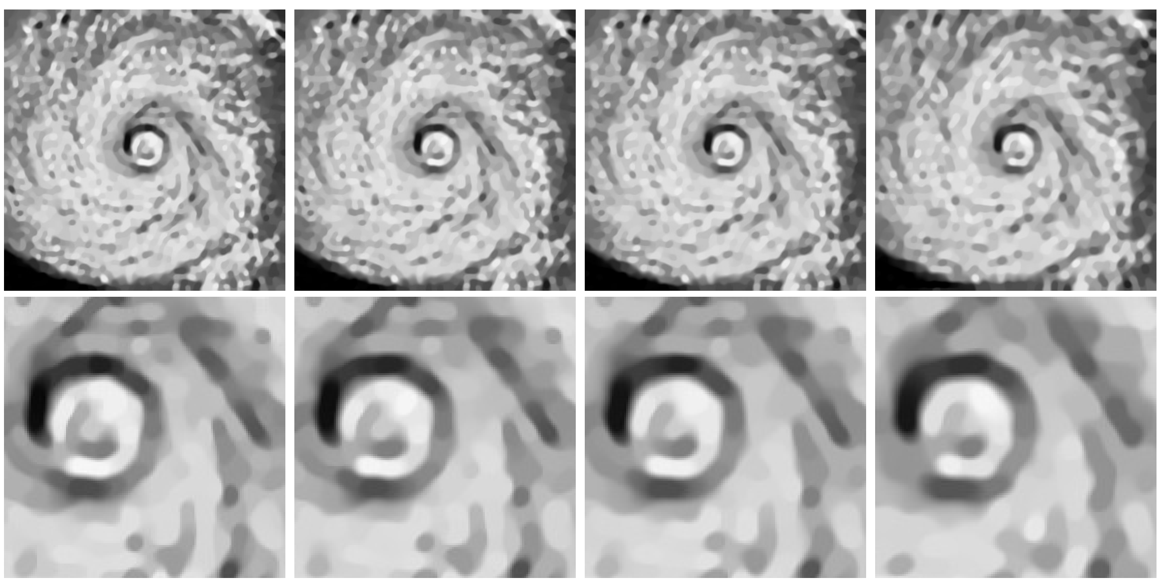

(a) Upsampling: $k = 2$ (b) Upsampling: $k = 3$ (c) Upsampling: $k = 4$ (d) Upsampling: $k = 8$

Fig. 10. Simultaneous Deconvolution and Upsampling results for images of Figure 9. All reconstructed images are 400x400. Upsampling factor is given by k. Full size images are shown on the first row, and zoomed in region of each image is shown in the second row. SNR and RMSE values for downsampled blurry images of Figure 9 and reconstructed images shown in this figure are listed in Tables III and IV, respectively.

each of the observations f_k can be expressed as

$$f_k = (K + s_k) * u_0 + \kappa_k,$$

where κ_k is image noise. The PSF noise s_k may be due to contribution from the time-varying thermal misalignment and constant alignment errors, among other error sources. A conceptual diagram of multiframe super-resolution process, which involves PSF degraded with different noise functions for each frame, is shown in Figure 12.

Availability of oversampled observations provides for data redundancy and can be used to decrease the effects of image noise and a noisy point spread function. The minimization problem for multiframe super-resolution we consider is

$$\min_u \quad ||u||_{TV} + \mu \sum_{k=1}^{Q} \omega_k ||K * u - f_k||_2^2, \tag{14}$$

where we choose the weighting constants ω_k using the total variation (TV) averaging [30]:

$$\omega_k = \frac{||f_k||_{TV}}{\sum_q ||f_q||_{TV}},$$

with $\sum_q \omega_q = 1$. The similarity term in (14) does not involve $s_k * u$ term; however, the averaging process reduces the

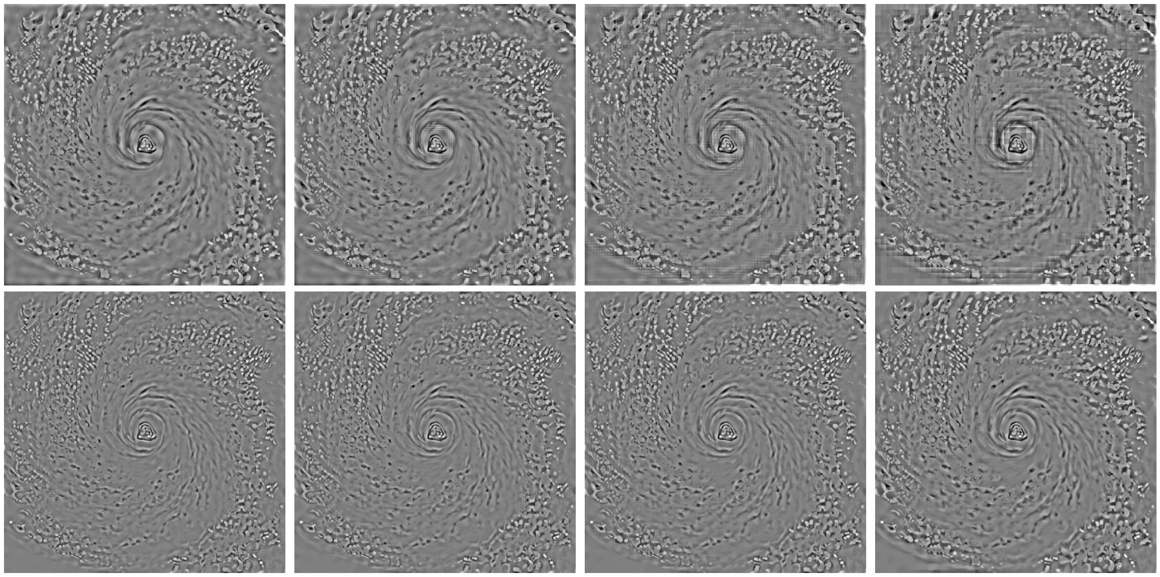

(a) Upsampling: $k = 2$ (b) Upsampling: $k = 3$ (c) Upsampling: $k = 4$ (d) Upsampling: $k = 8$

Fig. 11. First row shows errors in blurred, degraded by noise, and downsampled images from Figure 9. Second row shows errors in reconstructed images from Figure 10.

TABLE IV
ROOT MEAN SQUARE ERRORS (IN KELVIN) IN DOWNSAMPLED BLURRY AS WELL AS RECONSTRUCTED 150 GHZ IMAGES SHOWN IN FIGURES 9 AND 10

Downsampling factor	Downsampled blurry image	Reconstructed image
k = 1	20.46	14.85
k = 2	20.56	16.72
k = 3	20.72	17.53
k = 4	21.72	18.07
k = 8	22.97	19.65
k = 16	25.91	24.02

effective noise in a point spread function, as was shown in [31], [32]. We can re-write the minimization problem (14) as

$$\min_u \; ||u||_{TV} + \mu||K * u - \bar{f}||_2^2, \tag{15}$$

where $\bar{f} = \sum_k \omega_k f_k$ is the weighted TV mean of the observations f_k. The signal-to-noise ratio for an average image $\bar{f}$ will be larger than that for each f_k. In [30], the authors rigorously analyzed the advantages of using multiple degraded images for reconstruction. It was shown that while high spatial frequencies of f_k are contaminated by noise, the averaging process, such as TV averaging, reduces the amplitude of high frequencies in $\bar{f}$. Hence, the minimization problem (15) allows us to recover a wider range of frequencies of u_0 as the number of images increases. We apply fast Split Bregman deconvolution to (15) as was described in the previous section.

Figures 13 and 14 show the multiframe super-resolution results. Figure 13(a,b) shows a noisy GeoSTAR PSF corrupted with 10% visibility error. The clean image is consecutively blurred with the noisy PSF of this characteristic and is also corrupted with additive image noise of variance $\sigma^2 = 5K$ to produce a multiframe image sequence. The average signal-to-noise ratio of an image in the corrupted sequence is 5.93, and the average RMS error is 20.57. One of the corrupted images in a sequence is displayed in Figure 13(c). Super-resolution reconstruction results are shown in Figure 14 for cases when 3, 5, 10, and 20 frames are used. Table V shows signal-to-noise ratios and Table VI shows RMS errors of the reconstructed images. As expected, the quality of the reconstruction increases with the number of images in a sequence. Note that these errors – of 20 Kelvin for a single frame in Table VI – represent an extreme case for the purpose of illustration. The image noise requirement for the GeoSTAR instrument is 0.3 Kelvin RMS image error for each 15 minute image. The system

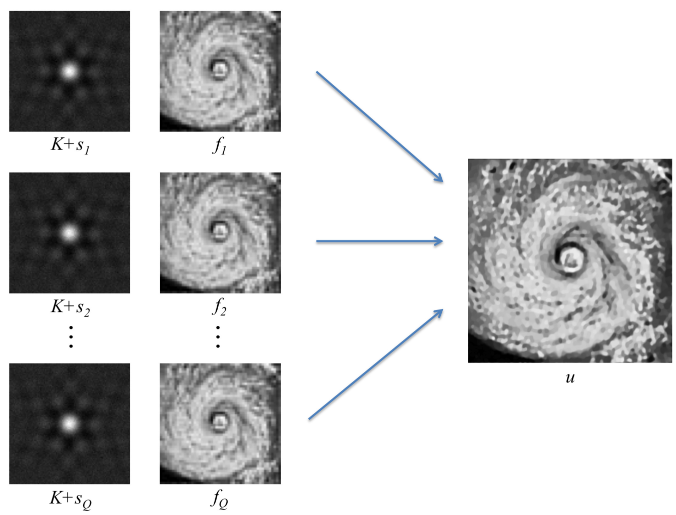

Fig. 12. Conceptual diagram of multiframe super-resolution process. A depiction of a physical scene, when captured, is convolved by the PSF K, degraded by a different noise function s_k, to arrive at the observation f_k. The super-resolution algorithm reconstructs image u from multiple observations.

TABLE V
SIGNAL-TO-NOISE RATIOS OF 150 GHZ IMAGE AFTER MULTIFRAME RECONSTRUCTION AS SHOWN FIGURES 14. FOR INITIAL FRAMES, AS IN FIGURE 13, SNRS ARE 5.93.

Number of frames	Reconstructed image
3	7.41
5	7.96
10	8.40
20	8.58

TABLE VI
ROOT MEAN SQUARE ERRORS (IN KELVIN) IN 150 GHZ IMAGE AFTER MULTIFRAME RECONSTRUCTION AS SHOWN IN FIGURE 14. FOR INITIAL FRAMES, AS IN FIGURE 13, RMS ERRORS ARE 20.57.

Number of frames	Reconstructed image
3	17.36
5	16.29
10	15.49
20	15.17

will be capable of observing shorter time intervals with the expectation that noise performance will degrade approximately by the inverse square root of observation time – but would never rise as high as 20 Kelvin (which would imply an observation interval of 0.2 seconds – which is much faster than any requirement).

VII. CONCLUSION AND FUTURE WORK

We developed efficient deconvolution and super-resolution methodologies and applied these techniques to reduce image blurring and distortion inherent in an aperture synthesis system. Unlike the conventional linear apodization approach, our process reduces not only the ringing within the image, but also significantly reduces the errors in the overall image. The deconvolution model was generalized to include the upsampling of images to a higher resolution grid. Furthermore, we developed an efficient multiframe super-resolution method which is robust to image noise and noise in the point spread function and leads to additional improvements in the spatial resolution.

There are several paths for future research. The most obvious one is to extend our methodology to multispectral framework, as we expect that combining multiple channels in the minimization procedures, rather than performing channel-by-channel minimization, would reduce errors in reconstruction. We also plan to enhance temporal resolution by accounting for physical deformation in consecutive frames while the scene is being captured. Ongoing and future work will also involve a broader study of performing simultaneous upsampling and deconvolution on real data. Finally, we plan to combine multiframe, multispectral, and simultaneous upsampling and deconvolution into a single computational framework.

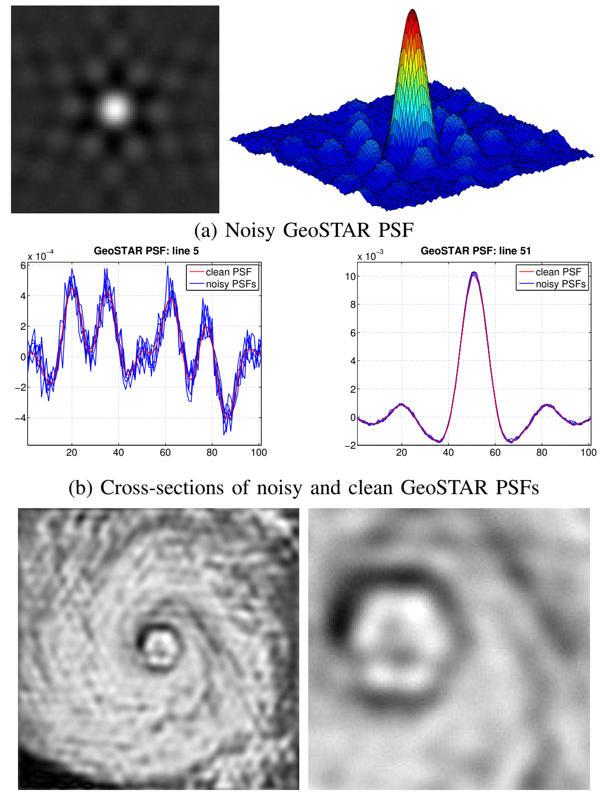

(a) Noisy GeoSTAR PSF

(b) Cross-sections of noisy and clean GeoSTAR PSFs

(c) Image blurred with noisy PSF from (a)

Fig. 13. (a) Noisy GeoSTAR PSF corrupted with 10% visibility error. (b) Two cross-sections of five noisy PSFs are compared with those of clean PSF. (c) Original simulated 150GHz image is blurred with noisy PSF from (a) and is further corrupted with additive image noise of variance $\sigma^2 = 5K$.

ACKNOWLEDGMENT

This research was carried out at the Jet Propulsion Laboratory, California Institute of Technology, under a contract with the National Aeronautics and Space Administration. The authors would like to thank Svetla Hristova-Veleva, Miyoun Jung, and Antonio Marquina for their helpful discussions and comments. They would also like to thank the anonymous reviewers for their useful suggestions in improving the quality of this paper.

REFERENCES

[1] A. Tanner, W. Wilson, B. Lambrigsten, S. Dinardo, S. Brown, P. Kangaslahti, T. Gaier, C. Ruf, S. Gross, B. Lim, S. Musko, S. Rogacki, and J. Piepmeier, "Initial results of the Geostationary Synthetic Thinned Array Radiometer (GeoSTAR) demonstrator instrument," *IEEE Transactions on Geoscience and Remote Sensing*, vol. 45, no. 7, pp. 1947–1957, 2007.

[2] A. Tanner and C. Swift, "Calibration of a synthetic aperture radiometer," *IEEE Transactions on Geoscience and Remote Sensing*, vol. 31, no. 1, pp. 257–267, Jan 1993.

[3] L. Rudin, S. Osher, and E. Fatemi, "Nonlinear total variation based noise removal algorithms," *Physica D*, vol. 60, pp. 259–268, 1992.

[4] L. Ambrosio and V. M. Tortorelli, "On the approximation of free discontinuity problems," *Bollettino Della Unione Matematica Italiana*, vol. B(7), pp. 105–123, 1992.

[5] P. Blomgren and T. F. Chan, "Color TV: Total variation methods for restoration of vector-valued images," *IEEE Transactions on Image Processing*, vol. 7, no. 3, pp. 304–309, 1998.

[6] L. Bar, A. Brook, N. Sochen, and N. Kiryati, "Deblurring of color images corrupted by impulsive noise," *IEEE Transactions on Image Processing*, vol. 16, no. 4, pp. 1101–1111, 2007.

[7] X. Bresson and T. F. Chan, "Fast dual minimization of the vectorial total variation norm and applications to color image processing," *Inverse Problems and Imaging*, vol. 2, pp. 455–484, 2008.

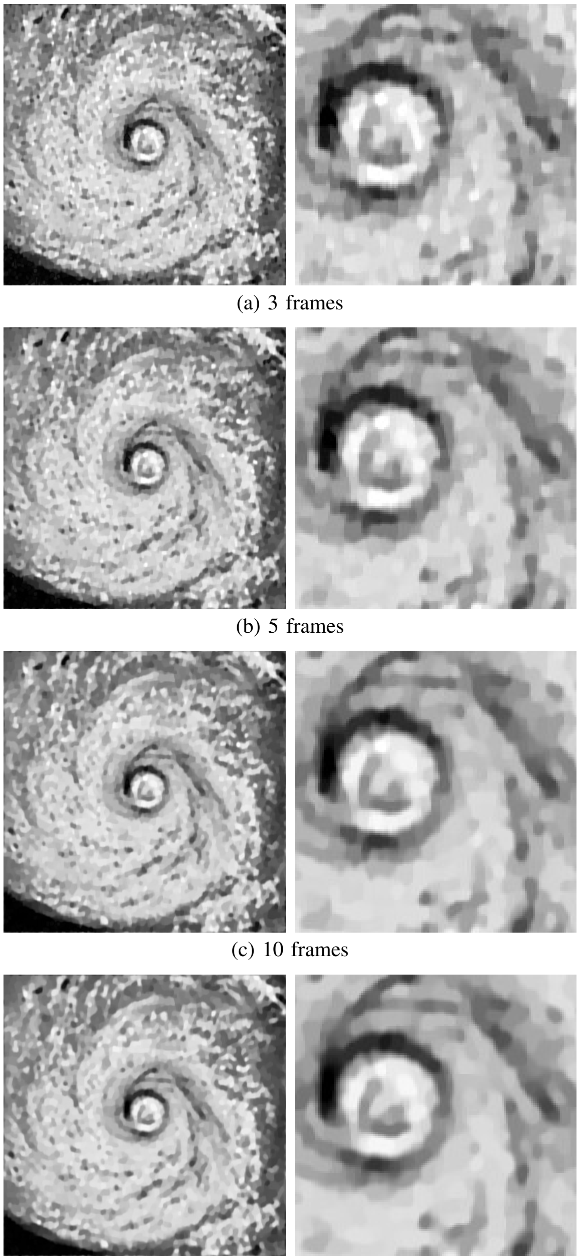

(a) 3 frames

(b) 5 frames

(c) 10 frames

(d) 20 frames

Fig. 14. Multiframe super-resolution results. Clean image is consecutively blurred with noisy PSF (one such PSF is shown in Figure 13(a)) and is also corrupted with additive image noise of variance $\sigma^2 = 5K$ to produce an image sequence. Super-resolution reconstruction results are shown for cases when 3, 5, 10, and 20 frames are used. SNR and RMSE values for reconstructed images are listed in Tables V and VI, respectively.

[8] G. Gilboa and S. Osher, "Nonlocal linear image regularization and supervised segmentation," *SIAM J. Multi. Model. & Simul.*, vol. 6, no. 2, pp. 595–630, 2007.

[9] ——, "Nonlocal operators with applications to image processing," *SIAM J. Multi. Model. & Simul.*, vol. 7, no. 3, pp. 1005–1028, 2008.

[10] G. Peyré, "Image processing with nonlocal spectral bases," *Multiscale Modeling & Simulation*, vol. 7, no. 2, pp. 703–730, 2008.

[11] A. D. Szlam, M. Maggioni, and R. R. Coifman, "Regularization on graphs with function-adapted diffusion processes," *Journal of Machine Learning Research*, vol. 9, pp. 1711–1739, 2008.

[12] Y. Lou, X. Zhang, S. Osher, and A. L. Bertozzi, "Image recovery via nonlocal operators," *J. Sci. Comput.*, vol. 42, no. 2, pp. 185–197, 2010.

[13] A. Buades, B. Coll, and J. M. Morel, "A review of image denoising algorithms, with a new one," *SIAM J. Multi. Model. & Simul.*, vol. 4, no. 2, pp. 490–530, 2005.

[14] S. Kindermann, S. Osher, and P. Jones, "Deblurring and denoising of images by nonlocal functionals," *SIAM J. Multi. Model. & Simul.*, vol. 4, no. 4, pp. 1091–1115, 2005.

[15] M. Jung, X. Bresson, T. F. Chan, and L. A. Vese, "Color image restoration using nonlocal Mumford-Shah regularizers," *Lecture Notes in Computer Science*, vol. 5681, pp. 373–387, 2009.

[16] ——, "Nonlocal Mumford-Shah regularizers for color image restoration," *IEEE Transactions on Image Processing*, vol. 20, no. 6, pp. 1583–1598, 2011.

[17] D. Mumford and J. Shah, "Optimal approximations by piecewise smooth functions and associated variational problems," *Communications on Pure and Applied Mathematics*, vol. 42, pp. 577–685, 1989.

[18] L. Rudin and S. Osher, "Total variation based image restoration with free local constraints," *IEEE International Conference on Image Processing*, vol. 1, pp. 31–35, 1994.

[19] Y. Wang, J. Yang, W. Yin, and Y. Zhang, "A new alternating minimization algorithm for total variation image reconstruction," *SIAM J. Imaging Sci.*, vol. 1, no. 3, pp. 248–272, 2008.

[20] J. Yang, W. Yin, Y. Zhang, and Y. Wang, "A fast algorithm for edge-preserving variational multichannel image restoration," *SIAM J. Imaging Sci.*, vol. 2, no. 2, pp. 569–592, 2009.

[21] T. Goldstein and S. Osher, "The split bregman method for L1-regularized problems," *SIAM J. Imaging Sci.*, vol. 2, no. 2, pp. 323–343, 2009.

[22] E. Candès, J. Romberg, and T. Tao, "Robust uncertainty principles: Exact signal reconstruction from highly incomplete frequency information," *IEEE Transactions on Information Theory*, vol. 52, no. 2, pp. 489–509, 2006.

[23] D. Donoho, "Compressed sensing," *IEEE Transactions on Information Theory*, vol. 52, no. 4, pp. 1289–1306, 2006.

[24] E. J. Candès, J. K. Romberg, and T. Tao, "Stable signal recovery from incomplete and inaccurate measurements," *Communications on Pure and Applied Mathematics*, vol. 59, no. 8, pp. 1207–1223, 2006.

[25] W. Yin, S. Osher, D. Goldfarb, and J. Darbon, "Bregman iterative algorithms for L1-minimization with applications to compressed sensing," *SIAM J. Imaging Sci.*, vol. 1, no. 1, pp. 143–168, 2008.

[26] S. Osher, M. Burger, D. Goldfarb, J. Xu, and W. Yin, "An iterative regularization method for total variation-based image restoration," *Multiscale Modeling & Simulation*, vol. 4, no. 2, pp. 460–489, 2005.

[27] D. L. Donoho and I. M. Johnstone, "Adapting to unknown smoothness via wavelet shrinkage," *Journal of The American Statistical Association*, vol. 90, no. 432, pp. 1200–1224, 1995.

[28] Y. Wang, W. Yin, and Y. Zhang, "A fast algorithm for image deblurring with total variation regularization," *CAAM Technical Report*, vol. TR07-10, 2007.

[29] J. Michalakes, J. Dudhia, D. Gill, J. Klemp, and W. Skamarock, *Design of a next-generation regional weather research and forecast model: Towards Teracomputing*. River Edge, New Jersey: World Scientific, 1998.

[30] A. Marquina and S. Osher, "Image super-resolution by TV-regularization and Bregman iteration," *J. Sci. Comput.*, vol. 37, pp. 367–382, 2008.

[31] M. Jung, A. Marquina, and L. Vese, "Multiframe image restoration in the presence of noisy blur kernel," *IEEE International Conference on Image Processing*, pp. 1529–1532, 2009.

[32] M. Jung, A. Marquina, and L. A. Vese, "Variational multiframe restoration of images degraded by noisy (stochastic) blur kernels," *J. Comput. Appl. Math.*, vol. 240, pp. 123–134, Mar. 2013.

Igor Yanovsky received the B.S. and M.A. degrees in 2002, and the Ph.D degree in applied mathematics in 2008, all from the University of California, Los Angeles, CA, USA.

He has been with the Jet Propulsion Laboratory, California Institute of Technology, Pasadena, CA, since 2008. He is also currently with the Joint Institute for Regional Earth System Science and Engineering, University of California, Los Angeles. His research interests are inverse problems and data analysis, particularly in areas of remote sensing, signal and image processing, computer vision, medical imaging, and atmospheric sciences.

Alan B. Tanner has worked as a microwave systems engineer at the Jet Propulsion Laboratory since 1989. He specializes in microwave radiometer and scatterometer design and calibration, and has lead the development of numerous ground and airborne instruments. These include the Advance Water Vapor Radiometers (AWVR) for the Cassini Gravitational Wave Experiment, the Airborne Cloud Radar (a 94 GHz scatterometer which preceded the CloudSat mission), the Airborne Rain Mapping Radar (built for validation of TRMM- or Tropical Rain Mapping Mission), and the Ultra Stable Microwave Radiometer, which was a NASA R&D instrument that formed the design basis for the Aquarius radiometer for ocean salinity measurements. Dr. Tanner is presently focused on the Geostationary Thinned Array Radiometer (GeoSTAR) development for microwave observations of the Earth from GEO. Dr. Tanner received his graduate degree from the University of Massachusetts at Amherst in 1989.

Bjorn H. Lambrigtsen joined the NASA Jet Propulsion Laboratory, California Institute of Technology, Pasadena, in 1982. He specializes in atmospheric remote sensing and related research. He is the GeoSTAR Principal Investigator and leads a number of other efforts as well, including hurricane-related research. He is a member of the NPOESS Preparatory Project science team, is the Microwave Instrument Scientist for the Atmospheric Infrared Sounder project, and leads the AIRS Atmospheric Science Group at JPL.

Luminita A. Vese received the M.S. degree in mathematics from West University of Timisoara, Romania, in 1993, and the M.S. and Ph.D. degrees in applied mathematics from University of Nice, Sophia, Antipolis, France, in 1992 and 1997, respectively. She is currently a Professor of Mathematics at the University of California, Los Angeles (UCLA). Before joining the UCLA faculty, she held postdoctoral research and teaching positions at the University of Nice, the University of Paris IX Dauphine, and UCLA. Her research interests include variational methods and partial differential equations, inverse problems, image analysis, and computer vision.